Design of MEMS-tunable novel monolithic optical filters in InP with horizontal bragg mirrors

Madhumita Datta [a,b,*], Marcel W. Pruessner [a,b], Daniel P. Kelly [a,b], Reza Ghodssi [a,b]

[a] *MEMS Sensors and Actuators Laboratory, Department of Electrical and Computer Engineering, The Institute for Systems Research, University of Maryland, College Park, MD 20742, USA*
[b] *The Laboratory for Physical Sciences, 8050 Greenmead Drive, College Park, MD 20740, USA*

Abstract

This paper presents the theoretical design and analysis of a tunable Fabry–Perot resonant microcavity filter realized by movable-waveguide-based integrated optical MEMS technology in InP. Wide-bandwidth, high-reflectivity horizontal InP/air-gap distributed bragg reflector (DBR) mirrors monolithically integrated with the waveguides have been proposed. The filter can be tuned by moving one of the high-reflectivity mirrors axially with on-chip MEMS electrostatic actuation. Spectral performance of the filter is numerically simulated taking into account the diffraction effects. Finite element mechanical modeling of the parallel-plate capacitive microactuator, consisting of a micromachined suspension beam and fixed electrodes, predicts a wide wavelength tuning range (1250–1650 nm) achievable by low actuation voltage (<7 V).
© 2004 Elsevier Ltd. All rights reserved.

1. Introduction

Micro-electro-mechanical systems (MEMS) provide a simple and useful broad wavelength-tuning mechanism by realizing variable-length Fabry–Perot (FP) resonant microcavities bound by two highly reflective mirrors in movable waveguide-based low-power photonic integrated circuits (PIC). Indium phosphide (InP)-based micro-opto-electro-mechanical systems (MOEMS) are particularly attractive for wavelength division multi-plexing (WDM) optical networks because of the possibility of integrating active and passive photonic devices in the wavelength region of 1250–1650 nm (the low-attenuation bandwidth of single-mode silica fibers). Coarse WDM (CWDM) network, which spans the entire wavelength spectrum of 1250–1650 nm, is increasingly gaining popularity in short-haul metro and access networks with high-bandwidth, protocol-transparent services [1]. The recently approved international standard for CWDM (ITU G.694.2) specifies 18 wavelength channels, centered on wavelengths from 1270 to 1610 nm, with a channel spacing of 20 nm. Thus, CWDM filters require a dynamic operating wavelength range of ~400 nm, and a 3-dB bandwidth (full width half maximum or FWHM) of <15 nm. Tunable InP MOEMS filters are key building blocks for reconfigurable CWDM

---
* Corresponding author. Tel.: +1-301-405-3729; fax: +1-301-314-9281.
 E-mail address: mdatta@umd.edu (M. Datta).

networks, as they relax manufacturing tolerances, and cut down on inventory costs.

To date, a variety of vertical MEMS-tunable filters have been reported in silicon [2], gallium arsenide [3], and InP [4]. Vertical devices are easier to fabricate, but they can not be monolithically integrated to an edge-emitting InP laser or waveguide. We are proposing a truly monolithic design for edge-emitting devices, where the mirrors and cavity of the FP filter are formed in line with the waveguides. The electrostatic actuator is also fabricated in a co-planar fashion, making the configuration suitable for fiber coupling.

2. Device configuration

In Fig. 1, we present the schematic of the proposed tunable filter. The microcavity is formed between the input and the output waveguides by fabricating novel monolithically integrated horizontal (i.e. in line with the waveguides) distributed bragg reflector (DBR) mirrors, which increase the effective facet reflectivity of the waveguides significantly. The length of the microcavity is varied to meet the Fabry–Perot resonant condition by moving one of the mirrors along the direction of propagation of the light. The input waveguide and mirror stack are rendered movable by etching away the sacri-
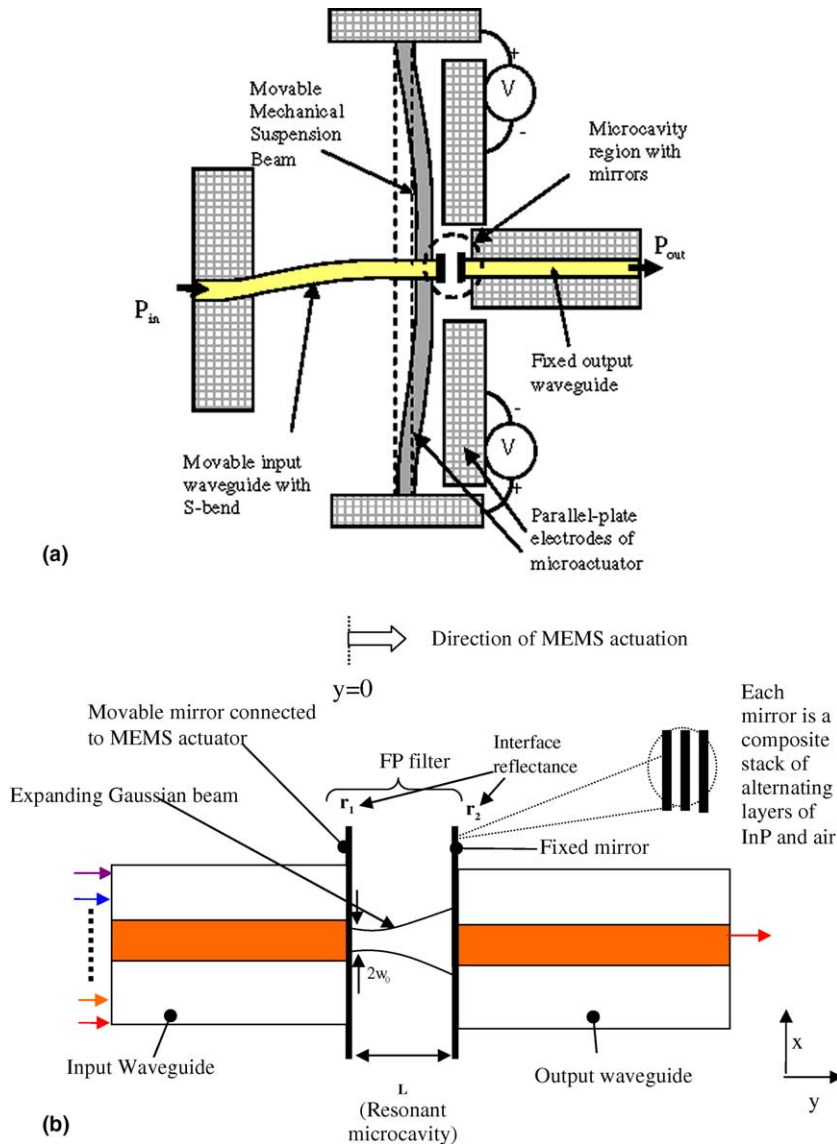

Fig. 1. (a) Schematic top view of the waveguide-based proposed resonant filter with the microcavity region circled; (b) details of the microcavity region magnified (actuator not shown).

ficial structural layer underneath it. The suspended input waveguide (and the mirror stack attached to it) is supported by a micromachined mechanical suspension beam, which can be electrostatically actuated by applying sufficient voltage between the electrodes. The waveguides, mirrors, and the suspension beam are monolithically fabricated on the same substrate using a single mask. The waveguide layers are doped moderately in order to enable electrostatic actuation. The parallel-plate capacitive microactuator consists of the suspension beam and the fixed electrodes. Fabry–Perot resonance condition is met when the microcavity length (L) is equal to an integral multiple of half-wavelengths in the cavity medium, i.e. $L = m\lambda_0/2n$, where $m = 1, 2, 3, \ldots$; λ_0 is the vacuum wavelength; and n is the refractive index of the cavity medium. The lithographically-defined initial microcavity length is set to transmit a single resonant wavelength when no voltage is applied. Applying precisely controlled voltage, the displacement of the front mirror is controlled, so that the filter can be continuously tuned within a wavelength range corresponding to the varying microcavity length. The input waveguide is curved to facilitate axial movement. The shape of the waveguide bend has been optimized (S-shaped bend with radius of curvature 1000 μm, and lateral shift 200 μm) to minimize radiation loss.

3. Optical design

3.1. Mirror design

In order to fabricate wide-bandwidth high-reflectivity mirrors enclosing the microcavity, we use micromachined semiconductor/air-gap DBR mirror structure [5], the schematic details of which are shown in Fig. 2 (before sacrificial etching). Alternating layers of semiconductor slabs (high-index material) and air-gaps-(low-index material) constitute each composite mirror, with the thickness of each layer (t_i) obeying the equation,

$$t_i = \left(\frac{2m + 1}{4n_i} \right) \lambda_0, \tag{1}$$

where $m = 0, 1, 2, 3, \ldots$; λ_0 is the vacuum wavelength; and, n_i is the refractive index of the ith layer. As the beam is mostly confined in the core, we have used $n_{core} = 3.192$ in designing the appropriate thickness of the semiconductor slabs corresponding to a nominal wavelength of $\lambda_0 = 1550$ nm. Refractive index of air, $n_{air-gap} = 1$.

Only three pairs of InP/air-gap layers in each mirror achieve an effective reflectivity of >95%, owing to the large refractive index contrast between the semiconductor and air. The mirrors are formed by lithographically defining hard mask patterns on the wafer, followed by dry-etching. First-order mirrors, (where $t_{core} = \lambda/4 = \lambda_0/4n_{core}$, and $t_{air-gap} = \lambda_0/4n_{air-gap} = \lambda_0/4$) are the most efficient, as they offer the highest reflectivity (>99%) and the highest bandwidth (>500 nm). However, e-beam lithography is required to fabricate first-order mirrors because of the nanometer-scale linewidths ($t_{core} = 121$ nm, $t_{air-gap} = 388$ nm) of the individual mirror slabs. A higher order mirror (e.g. $t_{core} = 7\lambda/4 = 847$ nm, and $t_{air-gap} = 3\lambda_0/4 = 1164$ nm) is structurally more stable and can be fabricated by optical lithography due to wider linewidths. The higher order mirror has lower peak reflectivity (~95%) and narrower high-reflectivity bandwidth (<300 nm), as shown in Fig. 3. Higher order mirrors reduce the filter's quality factor.
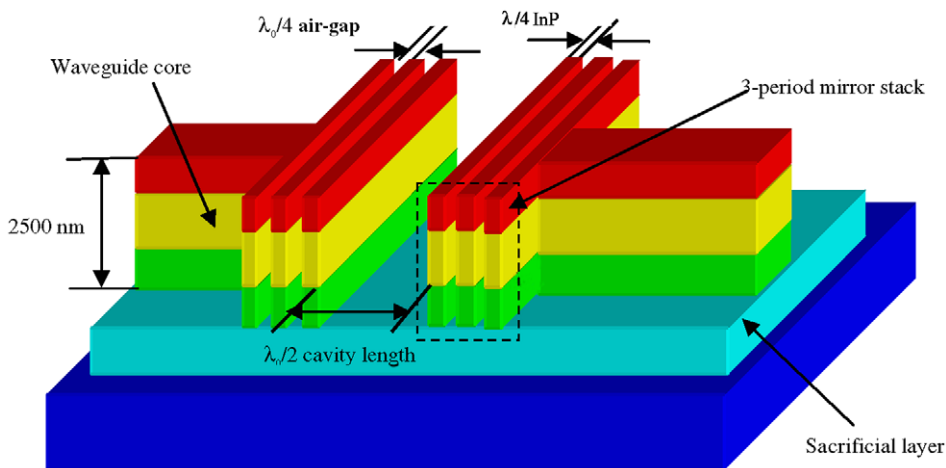

Fig. 2. Schematic of a filter with first-order mirrors (actuator not shown).
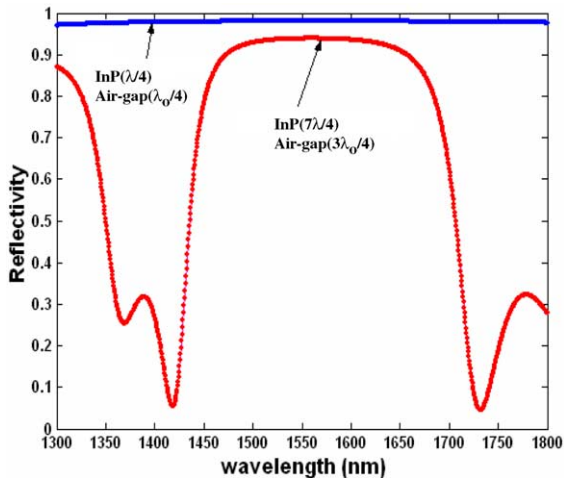
Fig. 3. Reflectivity spectrum of each of the three-period mirrors for different geometries.

3.2. Filter spectral response

Spectral response of the proposed resonant filter (Fig. 4a) has been numerically simulated using typical
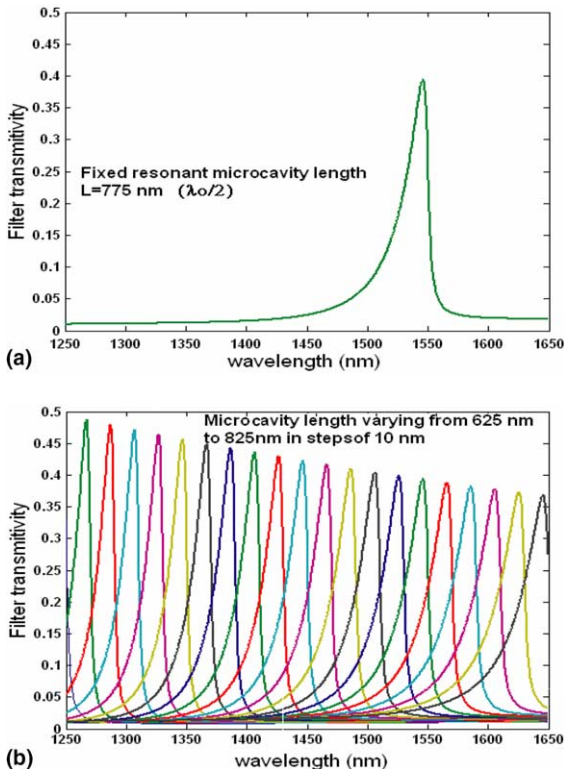

Fig. 4. (a) For fixed cavity length, the filter acts as a notch filter, allowing only one wavelength (λ_0) to pass. (b) The filter is made tunable for all the CWDM channels by varying the cavity length in steps of 10 nm.

values for monolithic input optical beam size (3 μm in lateral direction and 1.5 μm in vertical direction) and first-order mirror reflectivities. The effective transmittivity of the filter has been calculated using the tunable FP interferometer model developed by Aikio et al. [6]. Diffraction effects due to the expansion of the fundamental Gaussian beam within the unguided air-gap sections of the mirrors and the microcavity have been taken into account. Simulated diffraction-limited full width half maximum (FWHM) is 25 nm for single-stage filter. Spectral selectivity can be improved (FWHM ∼15 nm) by cascading two resonant microcavities, or by expanding the input beam. Fig. 4b shows that the filter can be tuned to any of the CWDM channel center wavelengths (1250–1650 nm, channel spacing 20 nm) by varying the half-wavelength microcavity length by a total of 200 nm in steps of 10 nm.

4. MEMS actuator design

The total axial displacement of the input mirrors is only +200 nm from the $y = 0$ position (the sign convention is such that when the movable mirror stack is pulled towards the fixed mirror stack, the displacement is positive), in order to achieve a wavelength tunability of 400 nm. The aim of the mechanical design is to ensure precision small-amplitude movement, achievable by the integrated parallel-plate capacitive microactuator shown in Fig. 1. When a voltage V is applied between the suspension beam and the fixed electrodes, a normal attractive force proportional to the square of the voltage acts on the beams, given by,

$$F_{\text{normal}} = \left(\frac{\varepsilon_0 w L}{2} \right) \frac{V^2}{(g_0 - d)^2}, \qquad (2)$$

where ε_0 is the free space permittivity, w is the thickness (depth) of the beam, L is the length of the beam (so that the product of 'wL' denotes the area normal to the attractive force), g_0 is the initial gap between the beam and the fixed electrode, and d is the displacement of the beam, linearly proportional to the balancing restoring force for small displacement range. For a doubly-clamped beam, the capacitive force acts as a uniform pressure load, and deforms the beam with the maximum displacement at the center and zero displacement at the two fixed ends (refer to Fig. 1(a)). Since the mirrors are located at the center of the suspension beam, we are interested in the maximum displacement of the suspension beam in response to the applied voltage.

We have simulated the design of the actuators using commercial Finite Element Analysis software ANSYS™ to obtain the required voltage for displacing the movable mirror stack axially by +200 nm. To reduce the stiffness constant of the suspension beam, a long beam
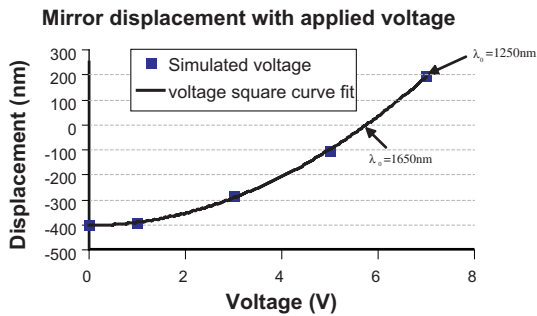
Mirror displacement with applied voltage

Fig. 5. Simulated actuation voltage for required mirror displacement.

length (800 μm) with spring-like serpentine structures at both ends has been considered. The moving mirror stack is supported symmetrically by the suspension beam in the *x* direction, but asymmetrically in the y direction, due to the presence of the input waveguide attached to it. In order to facilitate mirror movement in the *y* direction, the input waveguide is curved. The waveguide layers are designed with slight intrinsic tensile strain (<0.05%) to ensure that there is no out-of-plane movement during actuation. Upon sacrificial release, due to this intrinsic strain, the input waveguide and the suspension beam change shape to conform to its equilibrium position. At zero applied voltage, the mirror stack is pulled back by −400 nm (the suspension beam has a negative curvature at equilibrium). As the applied bias increases, the mirrors are attracted towards the fixed electrodes, making the microcavity length shorter. At approximately 5.7 V, the mirrors are at $y = 0$ position compensating the strain-induced pull-back, making the cavity length 825 nm, and allowing the 1650 nm wavelength to pass. At 7 V, the mirrors are displaced by +200 nm, i.e. cavity length becomes 625 nm (resonant wavelength 1250 nm). At this point the suspension beam has a positive curvature, as shown in Fig. 1(a) in an exaggerated way. The central mirror region, however, remains flat and parallel to the output mirrors due to the very large radius of curvature of the suspension beam. Fig. 5 plots the simulated displacement resulting from applying voltages 0, 1, 3, 5, and 7 V. The second-order

polynomial fit of the distinct data points confirms that the displacement is proportional to the square of the applied voltage (as expected theoretically).

5. Conclusions

We have presented the optical and mechanical design of an integrated MOEMS filter monolithically integrated on InP substrate, which achieves wide tunability of ∼400 nm, covering the entire CWDM spectral range. These low-operating voltage (<7 V) filters are attractive for dynamic wavelength demultiplexing with the possibility of integrating semiconductor optical amplifiers and photodetectors. Currently, these devices are being fabricated, and will be tested for spectral performance and loss measurements.

References

[1] Eichenbaum BR, Das SK. Economics for choosing a coarse WDM wavelength grid. Technical digest, National Fiber Optic Engineers Conference (NFOEC); 2001. p. 1444–8.

[2] Weiss SM, Fauchet PM. Electrically tunable silicon-based mirrors. In: Robbins DJ, Jabbour GE, editors. Silicon-based and hybrid optoelectronics IV. Proceedings of SPIE, vol. 4654. 2002. p. 36–44.

[3] Mateus CFR, Chang C-H, Chrostowski L, Yang S, Sun D, Pathak R, Chang-Hasnain CJ. Widely tunable torsional optical filter. IEEE Photonic Technol Lett 2002;14:819–21.

[4] Irmer S, Daleiden J, Rangelov V, Prott C, Romer F, Strassner M, Tarraf A, Hillmer H. Ultralow biased widely continuously tunable Fabry–Perot filter. IEEE Photonic Technol Lett 2003;15(3):434–6.

[5] Mukaihara T, Yamanaka N, Iwai N, Funabashi M, Arakawa S, Ishikawa T, Kasukawa A. Integrated GaInAsP laser diodes with monitoring photodiodes through semiconductor/air bragg reflector. IEEE J Sel Top Quant Electron 1999;5(3):469–75.

[6] Aikio J, Sidorin Y, Blomberg M, Karioja P. Wavelength tunable hybrid laser diode realized by using an electrostatically tuned silicon micromachined Fabry–Perot interferometer. In: Physics and simulation of optoelectronic devices VII. Proceedings of SPIE, vol. 3625. 1999. p. 588–97.